Journal of Materials Processing Technology 140 (2003) 432–440

Journal of Materials Processing Technology

www.elsevier.com/locate/jmatprotec

An elasto-plastic finite-element analysis of sheet metal camber process

You-Min Huang*, Tsung-Chia Chen

Department of Mechanical Engineering, National Taiwan University of Science and Technology, Taipei, Taiwan, ROC

Abstract

This study aims to clarify the process conditions of the V-die bending of a sheet metal of steel. It provides a model that predicts not only the correct punch load for bending, but also the precise final shape of products after unloading, based on the tensile properties of the material and the geometry of the tools used. An elasto-plastic incremental finite-element computer code, based on an updated Lagrangian formulation (ULF), was developed to simulate the V-die bending of sheet metal. In particular, selective reduced integration (SRI) was adopted to formulate the stiffness matrix. The extended *r*-minimum technique was used to deal with the elasto-plastic state and contact problems at the tool–metal interface. A series of experiments were performed to validate the formulation in the theory, leading to the development of the computer codes. The predicted value of the punch load in the finite-element model agrees closely with the results of the experiments. The whole deformation history and the distribution of stress and strain during the forming process were obtained by carefully considering the moving boundary condition in the finite-element method.

A special feature of this V-die bending process is the camber after unloading. The computer program successfully simulates this camber. The simulation was performed to evaluate the effects of the size of the blank and the bending angle on camber process. The effects of all process variables on the final bending angle of the bent parts of the sheet after unloading were also evaluated. Results in this study clearly demonstrated that the code for simulating the V-die bending process was efficient.

Keywords: Elasto-plastic; V-die bending; Camber; Spring-back

1. Introduction

Sheet-metal forming processes, including bending, stretching and drawing are extensively applied in industry, but the design of tools and the selection of sheet material almost always depend on trial and error, primarily because the shape of the tools, the characteristics of the material, the process variables and the geometrical configuration of the workpiece all influence the manufacturing process; these characteristics are difficult to formulate into a precise mathematical model. Sheet-metal bending is one of the most frequently applied sheet forming operations. Although the process is simple, the bending operation presents many technical problems of manufacturing. These include the prediction of spring-back or spring-forward after forming for tool design, control of the process or press, the accuracy of the component shape, the limitations of bendability, fractures originating from the stretched surface, and the estimation of the punch load of the V-die bending in press selection.

The die bending process is bending in a V-shaped die, so that the deformation shape follows from the punch's pressing the sheet into the die until it contacts with the sides of the die as much as possible. It is a non-steady state process that has two distinct phases—air bending and coining. Initially, the sheet passes through the air bending stage. The bending reaches a stage at which the edges of the bent sheet become tangent to the sides of the die near both support locations. At that moment, the coining stage begins. Coining has the purpose of removing the undefined state of plate curvature by forcing the plate to conform to the geometry of the punch–die system. The bending angle is forced to approach the die angle. After the bending process is completed, the punch is removed and the sheet returns to its final shape after unloading, at which residual stresses are in equilibrium. The unloading after forming strongly influences the final shape of products and becomes more complex following coining. In precise components of bending, the bend angle after unloading, i.e. spring-forward or spring-back, depends on process variables, including tensile properties, geometrical parameters and those of the coining process. Coining can reduce the spring-back or spring-forward of unloading during bending. Consequently, the unloading state after forming in V-die bending is hard to estimate. The conven-

* Corresponding author. Tel.: +886-2-2737-6487; fax: +886-2-2737-6460.
E-mail address: ymhuang@mail.ntust.edu.tw (Y.-M. Huang).

0924-0136/$ – see front matter © 2003 Elsevier B.V. All rights reserved.
doi:10.1016/S0924-0136(03)00741-6

tional prediction of an unloading state after forming does not apply to coining, as it is generally based on pure moment bending.

The V-bending of sheet metal has received little attention in the past, although the field has been extensively described [1]. Weinmann and Shippell [2] presented the results experiments on the V-die bending of a hot-rolled, high-strength, low-alloy steel sheet; both the maximum air bending force and the elastic unloading state in coining were assessed as functions of punch radius, die width and sheet thickness. Magnusson and Tan [3] used elementary bending theory with pure moment bending (no transverse stresses) to analyze V-die bending. An elasto-plastic incremental finite-element calculation [4,5] was performed to analyze the V-bending process with planar strain without friction, and to investigate spring-back and spring-forward phenomena. Additionally, the deformed geometry and stress distribution of the sheet were computed throughout the process until the unloaded state after forming was attained. Ogawa et al. [6] considered the accurate prediction of spring-back in a V-bending process without friction, using the finite-element method with element meshes of different sizes and comparing the results to those of experiments. The extended *r*-minimum method [7] was proposed to treat the contact problem during draw-bending. This scheme successfully handled the conditions at the interface between the sheet and the tool.

This work includes experimentation and finite-element simulations. An elasto-plastic finite-element computer code, based on an updated Lagrangian scheme, is adopted to simulate camber processes efficiently. A special feature of the scheme is the selective reduced integration (SRI) method [8], which has been proven to be efficiently applicable to nearly incompressible material. The method is used to treat the shell elements in the finite-element model. A modified Coulomb friction law was employed to treat the discontinuous alteration in the sliding–sticking state of friction at the contact interface. An extended *r*-minimum method was used to determine the dependence of the sheet-tool contact condition on deformation. The method is developed to describe the alternating sliding direction that occasionally increases computational difficulty. Experimental results concerning the V-die bending process were obtained for comparison with the results of the finite-element simulation to confirm the efficiency of the finite-element computer code.

2. Description of the basic theory

2.1. Material model

The following elasto-plastic constitutive equation for isotropic material is adopted to model the deformation behavior of the sheet.

$$\tilde{\tau}_{ij} = D^{\mathrm{ep}}_{ijmn}\dot{\varepsilon}_{mn} \tag{1}$$

where

$$D^{\mathrm{ep}}_{ijmn} = D^{\mathrm{e}}_{ijmn} - \frac{D^{\mathrm{e}}_{ijkl}D^{\mathrm{e}}_{uvmn}(\partial f/\partial\sigma_{kl})(\partial f/\partial\sigma_{uv})}{D^{\mathrm{e}}_{kluv}(\partial f/\partial\sigma_{kl})(\partial f/\partial\sigma_{uv}) + H'(\sigma_{uv}(\partial f/\partial\sigma_{uv})/\bar{\sigma})}$$

and D^{ep}_{ijmn} represents the coefficient of elasto-plasticity, D^{e}_{ijmn} is the coefficient of elasticity, $\tilde{\tau}_{ij}$ the Jaumann rate of Kirchhoff stress, $\dot{\varepsilon}_{ij}$ the rate of deformation, which is the symmetric part of the velocity gradient L_{ij} $(= \partial v_i/\partial X_j)$, X_j the fixed spatial Cartesian coordinate, σ_{ij} the Cauchy stress, H' the strain-hardening rate, f the yield condition of rate-independent strain-hardening plasticity and $\bar{\sigma}$ the effective stress.

2.2. Stiffness equation

The equation for virtual work can be made discrete. The updated Lagrangian formulation (ULF) in a framework of the application of an incremental deformation for the metal forming process (bulk forming and sheet forming) can be practically applied to describe the incremental properties of plastic flow. The current configuration according to ULF at each stage of deformation is used as a reference state to evaluate the deformation during a small time interval Δt, such that first-order theory is consistent with the required accuracy.

The rate equation for virtual work written as an updated Lagrangian equation [9] is

$$\int_V (\tilde{\tau}_{ij} - 2\sigma_{ik}\dot{\varepsilon}_{kj})\,\delta\dot{\varepsilon}_{ij}\,\mathrm{d}V + \int_V \sigma_{jk}L_{ik}\,\delta L_{ij}\,\mathrm{d}V = \int_{S_f} \dot{\bar{t}}_i\,\delta v_i\,\mathrm{d}S \tag{2}$$

in which v_i is the velocity, $\dot{\bar{t}}_i$ the rate of the nominal traction, and V and S_f represent the material volume and the surface on which the traction is prescribed.

Since the virtual work rate equation and the constitutive relation are linear equations of rates, they can be replaced with increments defined with respect to any monotonously increasing measure, such as the increase in the displacement of the tool.

Applying the standard procedure of finite elements to form the complete global stiffness matrix, yields

$$[K]\{\Delta u\} = \{\Delta F\} \tag{3}$$

in which,

$$[K] = \sum_{\langle e\rangle}\int_{V\langle e\rangle} [B]^{\mathrm{T}}([D^{\mathrm{ep}}] - [Q])[B]\,\mathrm{d}V + \sum_{\langle e\rangle}\int_{V\langle e\rangle} [E]^{\mathrm{T}}[G][E]\,\mathrm{d}V,$$

$$\{\Delta F\} = \left(\sum_{\langle e\rangle}\int_{S\langle e\rangle} [N]^{\mathrm{T}}\{\dot{\bar{t}}\}\,\mathrm{d}S\right)\Delta t$$

In these equations, $[K]$ represents the global tangent stiffness matrix, $[D^{ep}]$ the elemental elasto-plastic constitutive matrix, $[N]$ the shape-function matrix, $[B]$ the strain rate-velocity matrix, and $[E]$ is the velocity gradient-velocity matrix. The term $\{\Delta u\}$ represents the increment in nodal displacement and $\{\Delta F\}$ is the prescribed increase in nodal force. Matrices $[Q]$ and $[G]$ are defined as stress correction matrices associated with the stress states during each stage of deformation.

2.3. Formulating curvature

A three-dimensional analysis must consider the effectiveness of curvature. When the node moves, failing to consider the effectiveness of curvature would result in expecting unreasonable phenomena. Moreover, considering the effectiveness of curvature yields reasonable phenomena, in which the direction of the counter-force is orthogonal to the interface. Consequently, another item associated with curvature must be added to Eq. (3), yielding Eq. (4)

$$[K]\{\Delta u\} = \{\Delta F\} + \{\Delta C\} \tag{4}$$

where

$$\{\Delta C\} = F\Delta e = \hat{F}^{n+1} - \hat{F}^{n}$$

2.4. SRI formulation

The volume of a plastic medium is incompressible. Therefore, implementing the full integration technique for finite elements leads to over-strong constraint on thin plates. This phenomenon is caused by setting to zero the shear strains γ_{xz} and γ_{yz} during deformation [10]. The SRI procedure has been proven to treat effectively such problems as those involving volumetrically stiff contribution [11]. The generalized formulation of SRI due to Hughes [12] was used to develop the finite-element program in this study, which uses a four-node shell element.

The conventional strain rate-velocity matrix is decomposed into a dilational part (matrix $[B]_{dil}$) and the deviatoric part (matrix $[B]_{dev}$), such that $[B] = [B]_{dil} + [B]_{dev}$, in which $[B]_{dil}$ and $[B]_{dev}$ are integrated using conventional four-point integration.

The dilation matrix $[B]_{dil}$ is replaced by the modified dilation matrix $[\bar{B}]_{dil}$, which is integrated by one-point integration to determine the deformation of an almost incompressible elasto-plastic state. $[\bar{B}] = [\bar{B}]_{dil} + [B]_{dev}$ is used to generate the modified strain rate-velocity matrix $[\bar{B}]$, written as

$$[\bar{B}] = [B] + ([\bar{B}]_{dil} + [B]_{dil}) \tag{5}$$

The same procedure is used to formulate the modified velocity gradient-velocity matrix $[\bar{E}]$ rather than the velocity gradient-velocity matrix $[E]$

$$[\bar{E}] = [E] + ([\bar{E}]_{dil} + [E]_{dil}) \tag{6}$$

in which matrix $[E]_{dil}$ represents the dilational part of the velocity gradient-velocity matrix $[E]$ and $[\bar{E}]_{dil}$ is the modified dilation matrix of matrix $[\bar{E}]$.

3. Experiments and numerical analysis

This section discusses some experiments performed to verify the efficiency of the finite-element computer code in simulating the camber process. In the absence of some experimental results on the camber process, a finite-element simulation was run to examine the effects of the other process variables on the punch load and on the bend angle in the spring-back associated with the camber process. The experimental conditions, input data, analysis mode, boundary conditions, contact problems and unloading procedure after bending, are described below.

3.1. Experiments

Experiments were performed to examine the camber process and thus validate the developed finite-element model and computer code. China Steel Corporation supplied the experimental equipment and data on the material used. Fig. 1 depicts the profile of the die and punch head. The procedure followed in the experiments was as follows:

(a) Firstly, a metal sheet was manufactured precisely to yield a desired size of blank, and an electron microscope used to observe the microstructure of the piece, determining the rolling direction during manufacturing.
(b) The tool was assembled carefully on the pressing machine, and the punch and die were centrally calibrated and calibrated in parallel.
(c) The surfaces of the piece, punch and die were all coated with zinc stearate to reduce the friction between the metal piece and the tool, and also to increase the life of the tool.
(d) The punch speed was set to 1.0 mm/s.

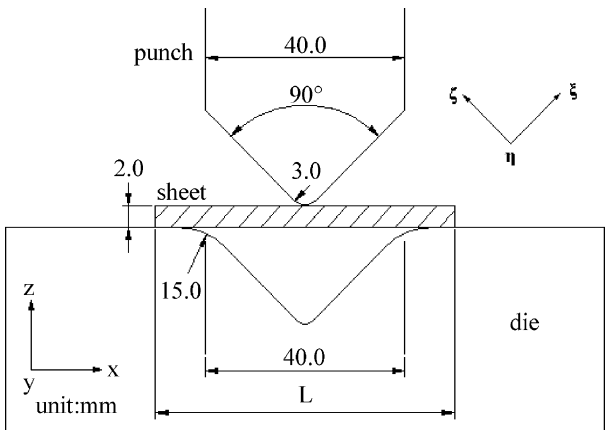

Fig. 1. The profile of the punch and the die.

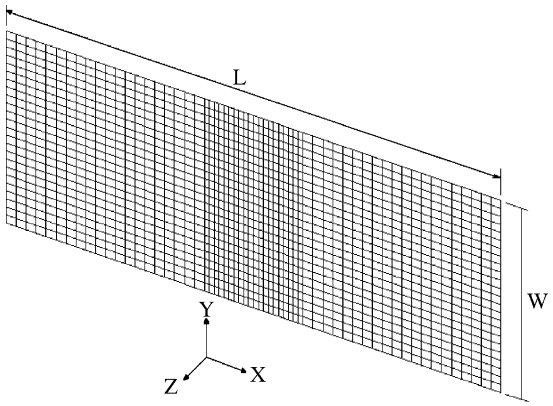

Fig. 2. The mesh of blank in camber forming simulation.

(e) The computer recorded the time and the relationship between the punch stroke and punch loading via data-gathering equipment.
(f) A coordinate measurement machine (CMM) was used to measure the camber and the bending angle of the sheet.

3.2. Numerical analysis

This work used a four-node rectangular shell element to derive a stiffness matrix and employed CAD software. The established tool and blank were meshed and transferred into a data file. The elasto-plastic large deformation 3D finite-element method was used to perform numerical analysis. The simulated punch load and punch stroke were compared with the corresponding experimental results, and the results of the analysis were output to CAD software to establish the deformation figure of stress and strain distribution. The above information can be used as a reference support designing a tool and its use in manufacturing.

China Steel Corporation provided the low carbon sheets used in the numerical simulation analysis. The tensile sheet specimens underwent standard tensile testing under continuous loading to failure. The least-square method was applied to approximate the true stress–strain relationship as a power law for work-hardening. The material data are as follows:

- thickness: $t = 2.0$ mm,
- yield stress: $\sigma_y = 291$ MPa,
- stress–strain: $\bar{\sigma}$ (MPa) $= 550.87(0.0135 + \bar{\varepsilon}_p)^{0.1483}$,
- Poisson's ratio, ν: 0.3,
- Young's modulus, E: 218 100 MPa.

In simulating camber forming, the finite-element mesh of the tool is triangular elements. Fig. 2 presents rectangular elements when the blanks are meshed. In simulating the blank, appropriate boundary conditions must be imposed. Conditions are set on the nodes such that the direction of rotation or displacement of nodes is constrained. In the simulation, the node on the X-axis of the blank constrained displacement in the Y-direction. The node on Y-axis of the blank constrained displacement in the X-direction. Additionally, the central node constrained the displacement in the X- and Y-direction and constrained the rotation in the Z-direction. Table 1 presents the data related to the tool and blank finite-element meshes, where L is 60.0 mm.

Table 1
Tool and blank finite-element meshes

Tool and blank	Element type	Node number	Element number
Punch	Triangle	1271	2400
Die	Triangle	1785	3400
Blank 1 ($W = 12.0$ mm)	Rectangle	793	720
Blank 2 ($W = 16.0$ mm)	Rectangle	1037	960
Blank 3 ($W = 24.0$ mm)	Rectangle	1525	1440

3.3. Boundary conditions

In forming a V-shape camber, the blank contacts the punch and die. Therefore, whether the node contacts or moves away from the tool must be determined. The node is classified as a contact node or a free node. Fig. 1 presents the boundary conditions pertaining to the combination of the blank and tool system. The node that does not touch the tool is defined as the free node, and its global coordinates are (X, Y, Z). The node that contacts the tool has local coordinates (ξ, η, ζ), following right-hand rule. Accordingly, Y and η are directed into the paper.

The contact, or otherwise, made by each node varies with the deformation of the blank. Therefore, during the calculation of the increase in displacement, the normal component of the contacting node force must be checked to determine whether it is less than or equal to zero. The next step in the calculation of the increase in the displacement must be changed; that is, the boundary condition of this node becomes that of a free node. The free node must also be checked to determine whether the contacts the tool. If so, in the subsequent step in the calculation of the increase in displacement, the boundary conditions are changed to those of a contacting node. The above calculation was performed with an extended r-minimum.

At the contact interface, the discontinuous alternation between the sliding and sticking states of friction occasionally causes computational difficulty; the treatment of the friction conditions requires special attention. A modified Coulomb friction law, proposed by Oden and Pries [13] and Saran and Wagoner [14], is assumed involving two contact friction states, sticking and sliding; this friction law effectively specifies the discontinuous variation in the direction of sliding. The camber process in the experiment is simulated by assuming a frictional coefficient of $\mu = 0.01$ to describe satisfactory lubrication and thus verify the developed finite-element method.

3.4. Treating the elasto-plastic and contact problems

The former boundary condition is such that the contact condition remains unaltered within one increment of deformation. Accordingly, the *r*-minimum method of Yamada et al. [15] was applied and extended to treat elasto-plastic and contact problems. The smallest of the following five values controls the increment in each loading step.

(1) *Elasto-plastic state*. When the stress of the Gaussian point of the element exceeds the yielding stress, r_1 is determined according to Ref. [15] to determine the stress just as the yielding surface is reached.
(2) *The maximum strain increment*. r_2 is obtained from the ratio of the default maximum strain increment $\bar{\alpha}$ to the principal strain increment $\mathrm{d}\varepsilon$; that is, $r_2 = \bar{\alpha}/\mathrm{d}\varepsilon$, to limit the incremental step to such a size that first-order theory is valid within the step.
(3) *The maximum rotation increment*. The rotation increment $\mathrm{d}w$ markedly influences the accuracy of the simulation during sheet bending. Consequently, r_3 is calculated as the ratio of the default maximum rotation increment $\bar{\beta}$ to the rotation increment $\mathrm{d}w$; that is, $r_3 = \bar{\beta}/\mathrm{d}w$, to limit the incremental step to such a size that first-order theory is valid within the step.
(4) *Penetration condition*. As forming proceeds, the free nodes of the sheet may penetrate the tools. The ratio r_4 [5] is calculated such that the free nodes just contact the tools.
(5) *Separation condition*. The nodes that come into contact with the tools may be separated from the contact surface because the sheet and tools that come into contact with each other do not adhere to each other. The ratio r_5 [5] is calculated for each contact node, such that the normal component of the nodal force is zero.

The maximum strain increment constant $\bar{\alpha}$ is 0.002 and the maximum rotation increment constant $\bar{\beta}$ is 0.5°. These constants are proven to be valid by first-order theory. Moreover, a small tolerance in the procedure for testing penetration and separation conditions is allowed.

According to the above conditions, *r*-minimum is the smallest value of r_1 to r_5

$$r_{\min} = \mathrm{MIN}\{r_1, r_2, r_3, r_4, r_5\}$$

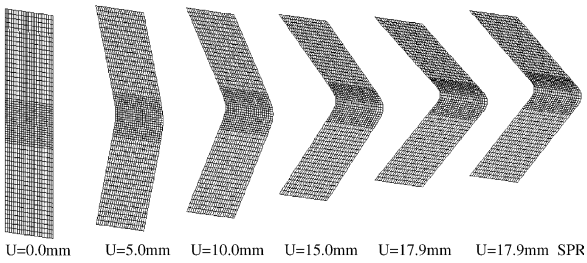

Fig. 4. The deformed geometry.

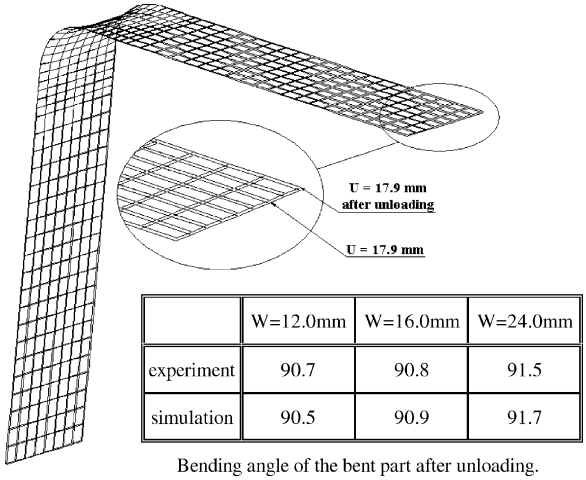

	W=12.0mm	W=16.0mm	W=24.0mm
experiment	90.7	90.8	91.5
simulation	90.5	90.9	91.7

Bending angle of the bent part after unloading.

Fig. 5. Experimental data and simulation results of spring-back angle after unloading at different width in a camber process.

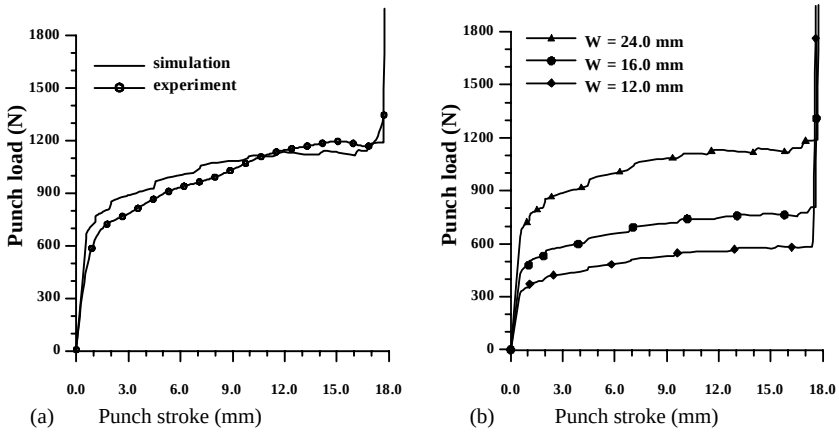

(a) (b)

Fig. 3. The punch load–punch stroke relationship.

The authors' previous work provides the formulation and solution algorithm [16].

3.5. Unloading process

Spring-back or spring-forward is significant in sheet forming; therefore, the unloading behavior following sheet forming is considered. The unloading procedure is executed, assuming that nodes on the center line (*Y*-axis) are fixed in the *X*-direction; all elements are reset to be elastic. The force with which the nodes contact the tools is reversed to become the prescribed force boundary condition on the sheet:

$$\Delta F = -F \tag{7}$$

All tools are removed during elastic unloading. The simulation program does not test the penetration, friction and separation conditions.

4. Results and discussion

The experiments and computation were performed until the punch load increased rapidly when most of the boundary of the sheet came into contact with the tool. Fig. 3(a) presents the relationship between the punch load and punch stroke in the blank ($W = 24.0$ mm) of camber process. The calculated relationship agrees closely with the experimental result. The simulated load matches the experimental results for loading; air bending proceeds during the early forming stage in which the punch load varies with the punch stroke, until the bend flange of the sheet touches the face of the die; then, the coining proceeds in the final bending stage in which the punch load increases even more quickly, since most of the boundary of the sheet touches the tools. Moreover, in Fig. 3(b), a larger width (*W*) corresponds to a greater required punch loading.

Fig. 4 plots the deformed geometries of the 90° bending process $W = 24.0$ mm in the five bending stages. This figure clearly shows that the sheet bends gradually until it enters the unloading state. At the contact interface, penetration, separation and friction throughout the bending process were accurately specified by the extended *r*-minimum method. Fig. 5 presents the experimental data and the simulation results for the spring-back angle in the camber process with various widths. The figure clearly shows satisfactory agreement between the simulation and the experiment. A larger width results in greater spring-back angle.

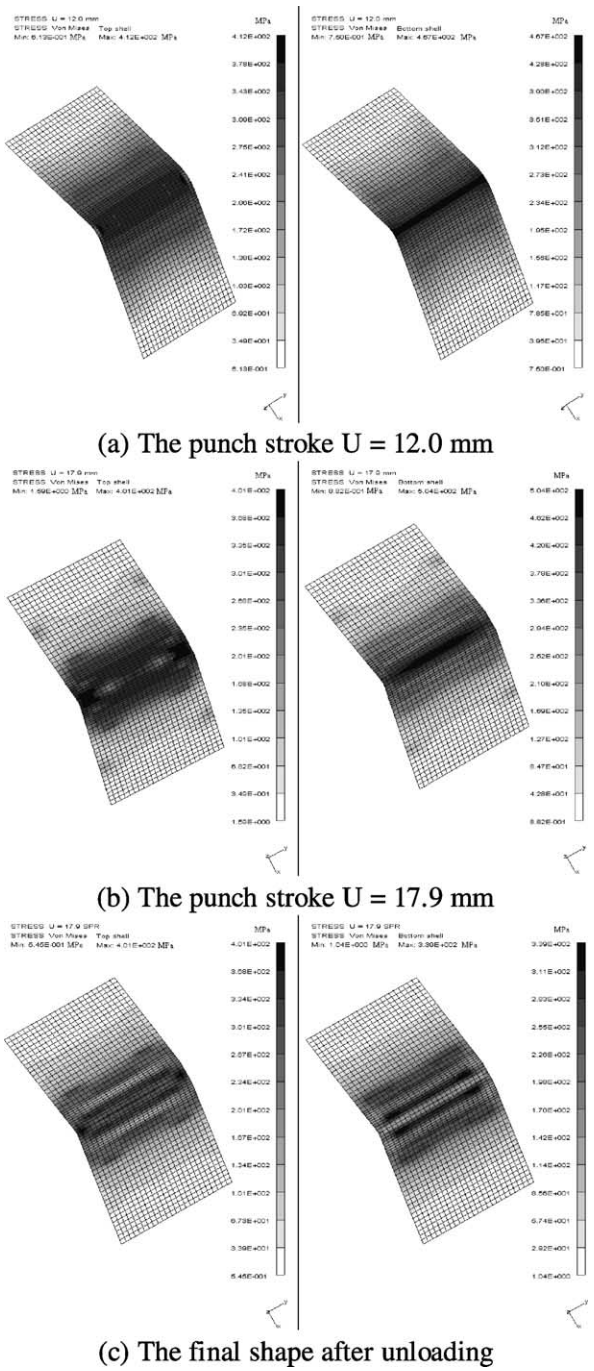

Fig. 6. The distribution of von Mises stress ($W = 24.0$ mm).

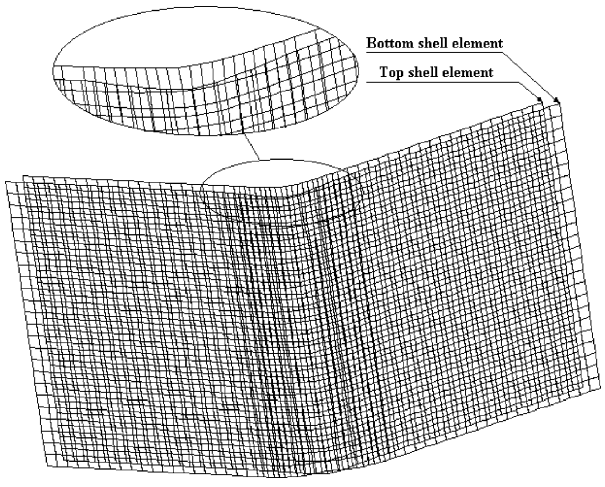

Fig. 7. The distortion situation on the two ends of *Y*-axis.

Fig. 6 shows the von Mises stress distribution for different punch strokes. The left-hand side of the figure presents the von Mises stress distribution of the top level shell elements. The right-hand side of the figure shows the von Mises stress distribution of bottom level shell elements. When the stroke reaches 12 mm, the top element, the stress of the two sides in the direction of the *Y*-axis is clearly a maximum. However, the stress on the bottom element increases from the two ends of the *Y*-axis toward to the center. In the final stage, when the stroke is 17.9 mm, the minimum stress of the top element is not at the center of *Y*-axis, but between the ends and the center. The stress is maximum near the two ends of the *Y*-axis. This situation is different with the stress distribution, which was obtained from sheet bending forming analysis by using pure moment bending. The stress on the bottom element is similar to that obtained in pure moment bending analysis. During unloading, the top element still has a large residual stress at the two ends of the *Y*-axis than elsewhere. The stress in the top element increases toward the two ends of the *Y*-axis, and the stress in the bottom element increases

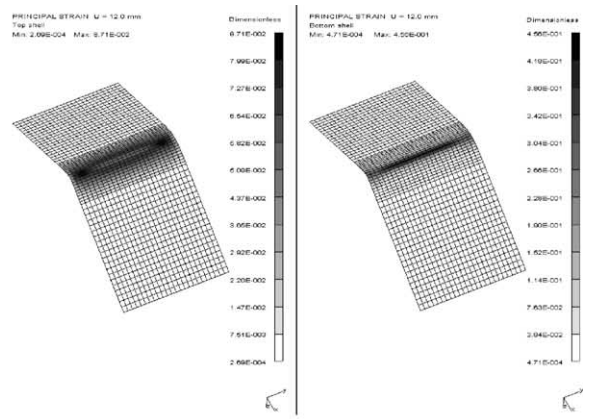

(a) The punch stroke U = 12.0 mm

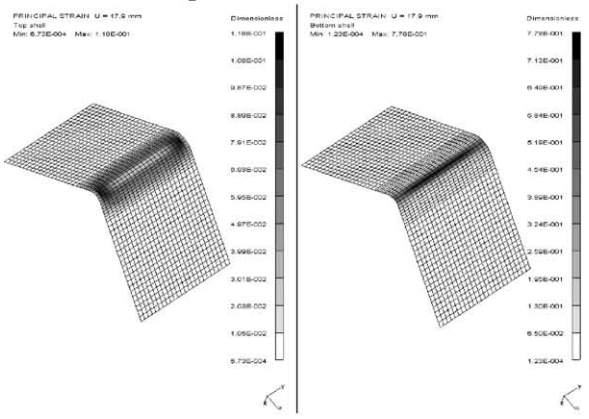

(b) The punch stroke U = 17.9 mm

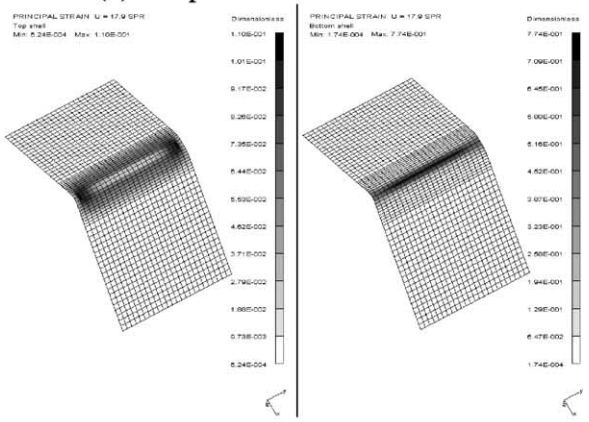

(c) The final shape after unloading

Fig. 8. Show the contour of the principal strain ($W = 24.0$ mm).

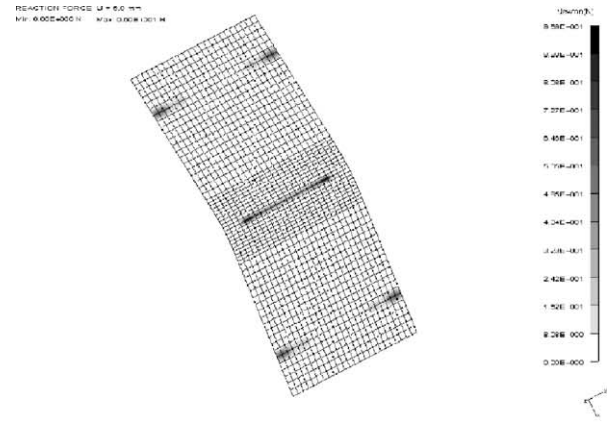

(a) The punch stroke U = 6.0 mm

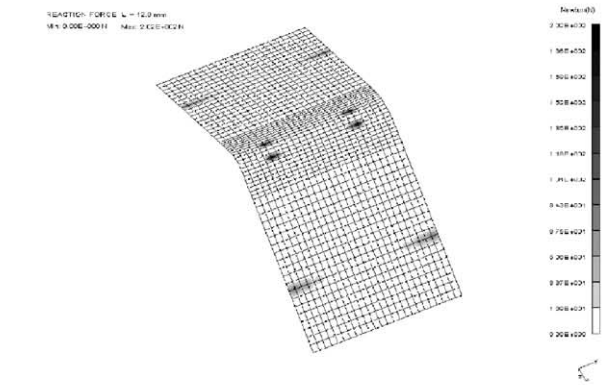

(b) The punch stroke U = 12.0 mm

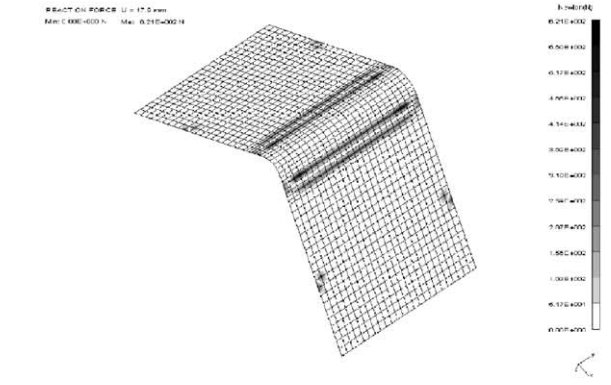

(c) The punch stroke U = 17.9 mm

Fig. 9. Reaction force distribution of different strokes.

toward the center of *Y*-axis. When the sheet undergoes bend forming, the camber shape appears. Fig. 7 shows the camber while the sheet undergoes bend forming. The camber is more clearly than the top element because the bottom element does not contact the die.

Fig. 8 shows the contours of the principal strain. The left-hand figure presents the principal strain distribution of the top shell element, and the right-hand figure presents that of the bottom shell element. When the stroke is 12.0 mm, the top element, the principal strain at the two ends of the *Y*-axis is clearly a maximum, and the principal strain in the bottom element increases closer to the center. In the final step, when the stroke is 17.9 mm, the top element, the principal strain is maximum near the two ends of *Y*-axis. The principal strain in the bottom element increases towards the center. In the unloading step, the principal strain in the top shell element remains largest at the two ends of the *Y*-axis. The contours exhibit a similar pattern: the maximum value is at the bottom of the sheet along the *Y*-axis, which is where the crack develops when the sheet is subject to large deformation during forming.

Fig. 9 plots the reaction force distribution of various strokes. The reaction distribution figure clearly shows the contact between the sheet and the tool. When the stroke is 6 mm, the top shell element on the *Y*-axis linearly contacts the punch. The bottom shell element contacts the die like a dot contact. When the stroke is 12 mm, the contact is like dot contact. When the stroke is 17.9 mm, the sheet touches the tool linearly on the *Y*-axis, proving that the bending forming reach coin step. Fig. 10 shows the thickness distribution during the unloading step. The thickness distribution figure shows that sheet is thinnest on the *Y*-axis. Consequently, if a crack exists, it must be on the *Y*-axis.

Fig. 11 shows the shape of camber for various strokes and different widths of sheet during sheet bending forming. When the stroke is 6 mm, the middle parts of the camber are a line while in sheets with different widths. The heights of the distortions at the two ends are the same. When the stroke is 12 mm, the middle parts of the camber are indented. Where the sheet is wider, the indentation is deeper. When the stroke is 17.9 mm, the middle part of the camber with $W = 12.0$ mm has a small indentation a little. When $W = 16.0$ mm, the indentation is greater and the middle part of the camber when $W = 24.0$ mm has the shape of a wave. Moreover, where the sheet is narrower, the shape of the camber is more obvious and the distortion is higher. When the sheet is wider, the camber takes on a wave-shape. The effects on the sheet bending forming are less, since the wave-shape situation is not conspicuous and the distortion is not very high.

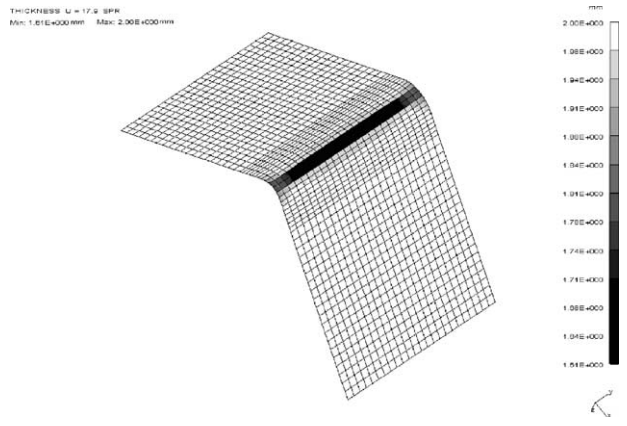

Fig. 10. The distribution of thickness after unloading.

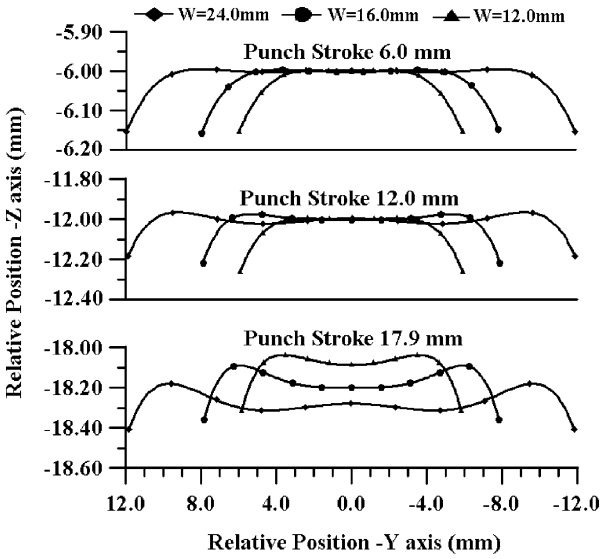

Fig. 11. In sheet bending forming, the camber shape in different strokes and different widths of sheets.

5. Conclusions

Experiments and theoretical computation are performed and the results compared to elucidate the camber process. Experiments were performed on commercial steel with a very well-lubricated punch and die. The theoretical computation employed the elasto-plastic large-strain finite-element method with selective reduced integration to develop the simulation program. The experiments and the finite-element model yield the following conclusions:

(1) The experimental results concerning the forming load from the initial shape to the final deformed V-shape agree very closely with the theoretical calculations, implying that the complete history of deformation can be traced successfully.
(2) The deformed geometry, the distribution of the stress and strain, and the bend angle are predicted effectively by the finite-element model. This information may be used to improve the manufacturing and design of tools.
(3) When the thickness is 2.0 mm, wider sheets result in a larger spring-forward angle.
(4) In bending processes, since the thinnest part of the sheet is on the *Y*-axis, if the crack exists, it must be on the *Y*-axis.

(5) When the sheet is narrower, the shape of the camber is clearer, and the camber is also higher. A wide sheet is associated with a wave-shaped camber.
(6) Since the tools are depicted using CAD software, the finite-element model can be applied to any arbitrary tool used in the workshop in general bending processes.

Acknowledgements

Authors want to thank scientists B.K. Lee and H.C. Xue, members of the Steel and Aluminium Research and Metallurgical Laboratory, China Steel Corporation, for valuable assistance in the experiments. The authors would like to thank the National Science Council of the Republic of China for financially supporting this research under Contract No. NSC 90-2212-E-011-041.

References

[1] K. Lange, Handbook of Metal Forming, McGraw-Hill, New York, 1985.
[2] K.J. Weinmann, R.J. Shippell, Effect of tool and workpiece geometries upon bending forces and springback in 90 degree V-die bending of HSLA steel plate, in: Proceedings of the Sixth North American Metal Working Research Conference, May 1978, pp. 220–227.
[3] C. Magnusson, Z. Tan, Mathematical modeling of V-die bending process, in: Proceedings of 16th Biannual IDDRG Congress, Stockholm, Sweden, May 1990, pp. 363–370.
[4] Y.-M. Huang, H. Takizawa, A. Makinouchi, T. Nakagawa, Elastic-plastic analysis of V-bending process, Spring Proceedings on Plastic Working, Cho-Fu, Tokyo, 1989, pp. 275–278.
[5] Y.-M. Huang, Y.H. Lu, A. Makinouchi, Elasto-plastic finite-element analysis of V-shape sheet bending, J. Mater. Process. Technol. 35 (1992) 129–150.
[6] H. Ogawa, A. Makinouchi, H. Takizawa, N. Mori, Development of an elasto-plastic FE code for accurate prediction of springback in sheet bending processes and its validation by experiments, in: Advanced Technology of Plasticity, Proceedings of the Fourth International Conference on Technology of Plasticity, 1993, pp. 1641–1646.
[7] A. Makinouchi, Finite element modeling of draw-bending process of sheet metal, in: Proceedings of the NUMIFORM'86 Conference, Gothenburg, 1986, pp. 327–332.
[8] D.S. Malkus, T.J.R. Hughes, Mixed finite-element methods—reduced and selective integration techniques: a unification of concepts, Comput. Meth. Appl. Mech. Eng. 15 (1) (1978) 63–81.
[9] R.M. McMeeking, J.R. Rice, Finite element formulations for problems of large elastic-plastic deformation, Int. J. Solids Struct. 11 (1975) 601–606.
[10] E. Hinton, D.R. Owen, Finite Element Software for Plates and Shell, Pineridge, Swansea, UK, 1984.
[11] T.J.R. Hughes, The Finite Element Method, Prentice-Hall, Englewood Cliffs, NJ, 1987.
[12] T.J.R. Hughes, Generalization of selective integration procedures to anisotropic and nonlinear media, Int. J. Numer. Meth. Eng. 15 (1980) 1413–1418.
[13] J.T. Oden, E.B. Pries, Nonlocal and nonlinear friction law and variational principles for contact problems in elasticity, Trans. ASME, J. Appl. Mech. 50 (1983) 67–76.
[14] M.J. Saran, R.H. Wagoner, A consistent implicit formulation for nonlinear finite element modeling with contact and friction. Part I. Theory, Trans. ASME, J. Appl. Mech. 58 (1991) 499–506.
[15] Y. Yamada, N. Yoshimura, T. Sakurai, Plastic stress–strain matrix and its application for the solution of elastic-plastic problems by the finite element method, Int. J. Mech. Sci. 10 (1968) 343–354.
[16] Y.-M. Huang, D.K. Leu, Finite element analysis of contact problems for a sheet metal bending process, Int. J. Comput. Struct. 57 (1995) 15–27.